A multi-colorimetric immunosensor for visual detection of ochratoxin A by mimetic enzyme etching of gold nanobipyramids

Hongshuai Zhu [1,2] · Chuanhe Liu [3] · Xinxin Liu [1] · Zhu Quan [1] · Weipeng Liu [1] · Yingju Liu [1,4]

Abstract

A multi-colorimetric immunosensor basing on the mimetic enzyme etching of gold nanobipyramids (Au NBPs) was established to detect ochratoxin A (OTA). Octahedral Cu_2O nanoparticles were successfully synthesized through a selective surface stabilization strategy, which can exhibit a peroxidase-like ability to oxidize 3,3′,5,5′-tetramethylbenzidine (TMB). Au NBPs can be etched by the product, TMB^{2+}, to form a significant longitudinal peak blue shift of local surface plasmon resonance. During the construction of the immunosensor, the microplate was coated with dopamine to immobilized OTA antigens, followed by the immunoreaction of OTA antibody and the Cu_2O-labled secondary antibody. A linear relationship can be found between the local surface plasmon resonance (LSPR) peak changes with the logarithm of OTA concentration in a wide range from 1 ng/L to 5 μg/L, while the detection limit was 0.47 ng/L. Meanwhile, the approximate OTA concentration can be conveniently and intuitively observed by the vivid color changes. Benefiting from the high specificity, the proposed multi-colorimetric immunoassay detection of OTA in millet samples was achieved, indicating the available potential of the immunoassay for the determination of OTA in real samples.

Keywords Multi-colorimetric immunoassay · Gold nanobipyramids · Octahedral Cu_2O · Local surface plasmon resonance · Ochratoxin A

Introduction

Colorimetric immunosensor has been extensively explored in rapid detection of food, pharmaceutics, and environment because of its low cost, excellent sensitivity, practicality, and simplicity [1]. Additionally, the colorimetric strategy generally relies on the visual judgment by naked eyes without the requirement of sophisticated equipment [2]. Although colorimetric immunoassay kits are already commercially available,

the majority of them can only be used for qualitative detection of the substances for the limited single color variation in response with different levels of targets (only intensity changes but no spectral peak shifts) [3, 4]. For instance, the extensively used 2,2′-azinobis-(3-ethyl-benzothiazoline-6-sulfonic acid) (ABTS)-horseradish peroxidase (HRP) immunoassay shows only a monochromic (blue) intensity change with microcystin-LR concentrations [5]. As we know that the optical density variations of the same color are not enough for semi-

Hongshuai Zhu and Chuanhe Liu contributed equally to this work.

✉ Weipeng Liu
  weipeng_liu@scau.edu.cn

✉ Yingju Liu
  liuyingju@hotmail.com

1 Key Laboratory for Biobased Materials and Energy of Ministry of Education, College of Materials and Energy, South China Agricultural University, Guangzhou 510642, China

2 The Guangdong Provincial Key Laboratory of Food Quality and Safety, College of Food Science, South China Agricultural University, Guangzhou 510642, China

3 Instrumental Analysis & Research Center, South China Agricultural University, Guangzhou 510642, China

4 State Key Laboratory of Managing Biotic and Chemical Treats to the Quality and Safety of Agro-products, Institute of Agro-product Safety and Nutrition, Zhejiang Academy of Agricultural Sciences, Hangzhou 310021, China

quantitative determination by naked eyes [6], it can be predicted that the accuracy of naked-eye judgment can be extremely enhanced as long as vivid colors appear with different concentrations of target molecules [7]. Therefore, it is urgent to develop a sensitive and multi-colorimetric immunoassay with color variations for quantitative or semi-quantitative detection of targets.

In recent years, noble metal nanomaterials have been widely applied in colorimetric immunoassay since the solution color is heavily reliant on their composition, shape, and size [8–10]. For example, gold nanorods (Au NRs)-based colorimetric immunoassay has been a cause for concern due to their extremely controllable shapes and tunable peaks of localized surface plasmon resonance (LSPR) [11, 12]. The longitudinal LSPR of Au NRs is located in the visible near-infrared range [13]. Especially, different aspect ratios of Au NRs can cause a range of colors for visual detection, since the longitudinal LSPR peak can shift to shorter characteristic wavelength (blue shift) when the aspect ratio decreases [14]. However, due to the round-end structure of Au NRs, the color change is not obvious at a low concentration [15]. Compared with Au NRs, the aspect ratio of plasmonic gold nanobipyramids (Au NBPs) is more easily to be changed, owing to its two sharper apexes [16]. Consequently, the Au NBPs-based immunoassay not only promotes the sensitivity but also displays a range of individual colors as colorful as a rainbow.

Ochratoxin A (OTA) is secreted by *Penicillium* and *Aspergillus fungi*. It can be found in agricultural products, food, and feedstuffs such as rice, peanut, coffee, dried fruits, corn, beer, and wine [17, 18]. Meanwhile, due to its high chemical and thermal stability, it can enter the animal body and invade human blood and breast milk [19, 20]. For such reasons, OTA can not only cause economic loss in agriculture production but also post a threat to the animal and general population health, since it can generate toxic effect on the liver, kidney, and immune modulatory system [21, 22]. Therefore, the International Agency for Research on Cancer (IARC) has listed OTA as a potential carcinogen (group 2B) for human beings [23]. Consequently, the real-time quantitative determination of OTA is a key challenge for human health and food safety. To date, traditional methods are used to monitor and detect OTA, which mainly include high-performance liquid chromatography (HPLC) [24, 25], thin-layer chromatography [26], and liquid/gas chromatography-tandem mass spectrometry (GC/LC-MS) [25, 27]. However, such methods are still restricted, owing to the expensive cost, trained personnel, low sensitivity, and complicated pre-treatment of samples. Therefore, in order to keep the humans and animals' food chain away from the OTA contamination, a simple, rapid, and sensitive detection strategy for OTA is needed.

In this work, Cu_2O octahedrons were successfully synthesized through a selective surface stabilization strategy, showing the peroxidase-like activity to catalyze TMB. As for the immunoassay, the microplate was coated with dopamine to immobilize antigens, followed by the immune response with OTA antibody and the Cu_2O-labled secondary antibody. The concentration of OTA was relative with the amount of Cu_2O nanoenzyme, which can further affect the amount of TMB^{2+}. Finally, by etching Au NBPs from different amount of TMB^{2+}, the Au NBPs mixture can generate vivid color response. Therefore, the OTA concentration can be conveniently judged by the naked eyes and LSPR shifts.

Experimental section

Materials and instruments

Sodium hydroxide (NaOH), cupric chloride dihydrate ($CuCl_2 \cdot 2H_2O$), hydrochloric acid, ascorbic acid (AA), sodium acetate, $NH_3 \cdot H_2O$ (25%), sodium citrate, $AgNO_3$, H_2O_2 (30%), TMB, and $NaBH_4$ were received from the Aladdin Biological Technology Co. Ltd. (China, www.aladdin-e.com). Tween and dopamine hydrochloride were obtained from the Shanghai Acros Organics (China, www.acros.com). Polyvinylpyrrolidone (PVP, MW: 40, 000) was bought from the Beijing Solarbio Science & Technology Co. Ltd. (China, www.solarbio.com), while 3-aminopropy trimethoxysiane (APTES), hexadecyl trimethyl ammonium chloride (CTAC), and chloroauric acid ($HAuCl_4$) were purchased from the Macklin Biochemical Co. Ltd., Shanghai (China, www.macklin.cn). Hexadecyl trimethyl ammonium bromide (CTAB) was purchased from the Shanghai Adamas Reagent Co. Ltd. (China, www.adamas.com). The secondary goat anti-rabbit antibody (Ab_2, 1 mg/mL) was purchased from Santa Cruz (China, www.scbt.com). The antibody of ochratoxin A (Ab_1, 1 mg/mL) and the antigen of OTA (antigen, 2 mg/mL) were obtained from the College of Food Sciences, South China Agricultural University. Typically, sodium acetate-acetic acid buffer (HAc-NaAc) of different pH was obtained by mixing acetic acid at specific ratios. The washing buffer of the immunosensor was 10 mM of PBS (pH 7.4) with 0.5% tween-20 (PBST).

Scanning electron microscopy (SEM, Talos F200S, Thermo Fisher, USA) and transmission electron microscopy (TEM, Talos L120C, Thermo Fisher, USA) were used to characterize the morphologies of nanomaterials, while Fourier infrared spectrometer (FTIR, IS-10, Thermo Fisher, USA), energy-dispersive spectrometer (EDS, Thermo Fisher, USA), and X-ray diffraction (XRD, D/max-IIIA, Japan) were used to discover the functional groups, the element, and structure analysis of nanomaterials. The absorption spectrum was determined by UV-visible spectrophotometer (Evolution 220, Thermo Fisher, USA). The photographs of the reaction wells were taken with an iPhone 6s plus.

Preparation of the Cu$_2$O@Ab$_2$ conjugate

As shown in Fig. S1, in a typical procedure, 0.3333 g polyvinylpyrrolidone (PVP, M_w 40 000) was dissolved into 100 mL CuCl$_2$·2H$_2$O solution (0.01 M) by ultrasonic dispersion. Afterwards, 10.0 mL NaOH aqueous solution (2.0 M) was drop-wise added. In this process, the solution color changed from transparent light green to turbid blue-green and then gradually dark brown. After the solution was stirred for 30 min, 10 mL of AA solution (0.6 M) was added. The above mixture was aged for 25 min, followed by the formation of a turbid red liquid. All of the synthesis was conducted under constant stirring in a water bath at 55 °C. After that, it was cooled naturally to 25 °C, and then the resulting product was obtained by centrifugation, followed by washing with ethanol and water to remove the residual inorganic ions and polymer. The final Cu$_2$O nanoparticles were dried at 60 °C for 3 h for further use.

Then, a mixture of octahedral Cu$_2$O (0.01 g) and 3-aminopropy trimethoxysiane (APTES, 600 µL) was gradually added into 10 mL of ethanol/water mixture (19:1, v/v), dispersed ultrasonically for 20 min, and then heated at 75 °C for 1 h, followed by washing with ethanol to remove the redundant APTES. Then, 1.5 mL of aminated Cu$_2$O nanoparticles were homogeneously dispersed into 1 mL of PBS buffer (pH 7.4, 0.01 M). After adding 1 mL of 2.5% glutaraldehyde, the solution was incubated for 2 h at room temperature, followed by rinsing, re-dispersion, and adding 5 µL of Ab$_2$ (1 mg/mL). After stirring for 24 h at 4 °C, centrifugation, and purification, the precipitate was dispersed in PBS buffer (1 mL) for further use. Consequently, the labeled Cu$_2$O@Ab$_2$ was synthesized by the crosslinking reaction of the amino groups of the Ab$_2$ and the amino-functionalized Cu$_2$O in the presence of glutaraldehyde [28].

Preparation of Au NBPs

A seed-mediated growth strategy was used to synthesize Au NBPs with little modifications [29]. Firstly, a 10 mL mixture including citric acid (5 mM), HAuCl$_4$ (0.25 mM), and CTAC (50 mM) was prepared, followed by the addition of freshly prepared ice-cold NaBH$_4$ (0.25 mL, 25 mM). It was stirred constantly for 90 min at 80 °C until its color became burgundy, indicating that the gold seeds were synthesized. Secondly, a solution containing AgNO$_3$ (10 mM, 2 mL), HAuCl$_4$ (10 mM, 10 mL), HCl (1 M, 4 mL), CTAB (100 mM, 200 mL), and AA (0.1 M, 1.6 mL) was prepared and stirred vigorously, followed by the addition of 10 mL of gold seeds and stirring at 30 °C for 2 h. Then, the mixture was centrifuged and dispersed in 150 mL CTAC (80 mM), followed by the injection of 20 mL AA (0.1 M) and 40 mL AgNO$_3$ (10 mM). After heating at 65 °C for 4 h, the product was collected by centrifugation, dispersed in 150 mL CTAB (100 mM), and left

at room temperature overnight. After the removal of the supernatant, the precipitates were redistributed into 100 mL ultrapure water, and then 10 mL NH$_3$·H$_2$O (25 wt%) and 1 mL H$_2$O$_2$ (5 wt%) were added into the above solution at room temperature for 4 h. After centrifugation and washing, Au NBPs were obtained and redispersed in 100 mL CTAB (1 mM) solution.

Construction of the multi-colorimetric immunosensor

In brief, 1 mg/mL of dopamine (50 µL) was added into the wells of the microplate. After incubation for 0.5 h at 37 °C and drying, 30 µL of the antigen (10 µg/mL) was added into each well and incubated at 4 °C. Then, 30 µL of the blocking solution was injected to seal up the rest points. Based on the competitive immunosensor, 30 µL of the mixture solution including particular volume of Ab$_1$ (5 µg/mL) and different concentrations of OTA were injected into the appropriate wells. After that, 30 µL of the Cu$_2$O@Ab$_2$ solution was added and incubated for 1 h at 37 °C. After washing with PBST, 200 µL HAc-NaAc buffer (pH 6.0, 0.2 M), 30 µL TMB (30 mM), and 50 µL H$_2$O$_2$ (70 mM) were sequentially injected and reacted for 5 min at room temperature, causing the color change from TMB (colorless) to TMB$^+$ (blue). After the injection of 50 µL HCl solution (1 M), the TMB$^+$ was oxidized to form the yellow diimine oxidation product of TMB^{2+}. Finally, the TMB^{2+} solution was added into 200 µL Au NBPs solution. After etching for 18 min at room temperature, the color of the mixture was recorded by an iPhone 6s plus. Simultaneously, the absorption spectra were tested in the range of 300–800 nm by a UV-visible spectrophotometer.

The millet sample was pretreated as follows. 4 g of millet was added into 20 mL mixture of acetic acid, water, and acetonitrile (1:20:79, v/v/v). The sample was mixed by shaking for 30 s and then sonicating for 30 min. The filtrate was collected by using nylon-66 membranes (0.22 µm). The extraction was conducted twice.

Results and discussion

Characterization of the Cu$_2$O@Ab$_2$ conjugate

In this work, Cu$_2$O octahedrons were synthesized with geometry control through a selective surface stabilization strategy [30]. The broad views of Cu$_2$O octahedrons at different scales were shown in Fig. 1a and b. The results showed that smooth Cu$_2$O octahedrons were in 3D symmetry pyramidal structure with regular shapes and uniform sizes. The unique structure was beneficial to disperse in solution and anchor colorimetric substrates. Meanwhile, in Fig. 1c, the particle size analysis further proved that Cu$_2$O octahedrons presented a sharper size
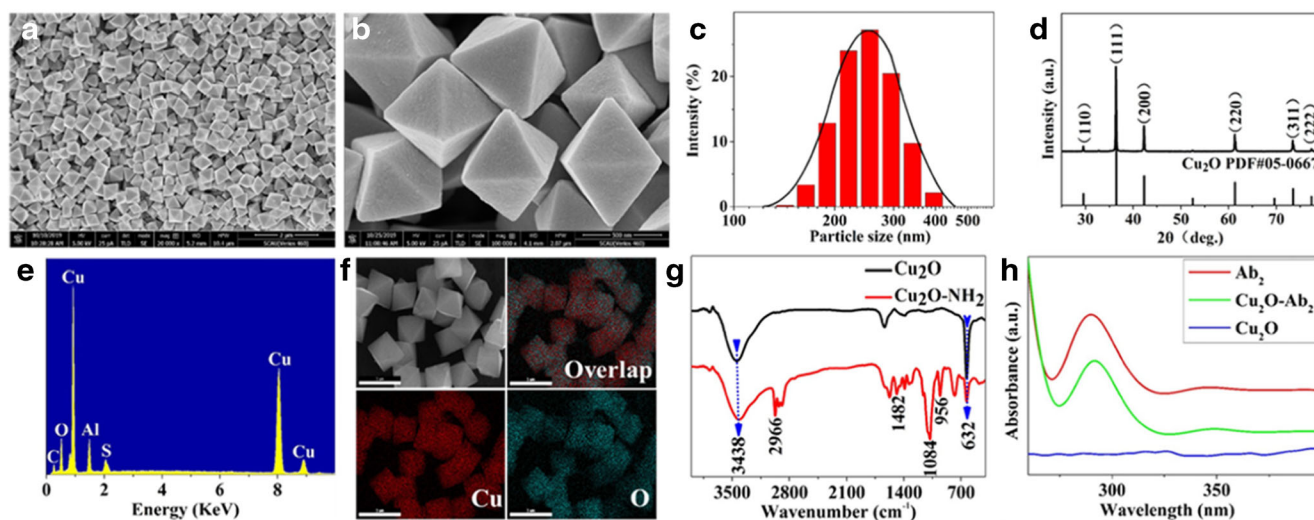
Fig. 1 SEM images of Cu₂O octahedrons (**a**, **b**) at different magnifications. (**c**) Particle size distribution, (**d**) XRD, (**e**) EDS, and (**f**) elemental mapping of Cu₂O octahedrons. (**g**) IR spectra of Cu₂O octahedrons and aminated Cu₂O octahedrons. (**h**) UV-vis spectra of Cu₂O octahedrons, Ab₂ and Cu₂O-Ab₂

distribution of 245 nm in average. The narrow size distribution of nanoparticles can guarantee a high catalytic activity.

The crystallinity of Cu₂O octahedrons was investigated by X-ray diffraction (XRD). In Fig. 1d, the diffraction peaks at 2θ angles of 29.6°, 36.4°, 42.3°, 61.3°, 73.5°, and 77.3° corresponded to crystal planes (110), (111), (200), (220), (311), and (222), respectively (JCPDS 05-0667), suggesting that Cu₂O nanoparticles exhibited a cubic phase. Not any impurity can be discovered, indicating the successful synthesis of Cu₂O octahedrons. The energy-dispersive spectrometry (EDS) revealed that the sample was mainly composed of Cu and O atoms (Fig. 1e). In order to further understand the component of Cu₂O octahedrons, elemental mappings (Fig. 1f) demonstrated that elements of Cu and O were evenly distributed on the surface. As shown in the FTIR spectrum of Cu₂O octahedrons (Fig. 1g), the broad band at 3438 cm⁻¹ was attributed to the -OH stretching vibration of absorbed surface water, while the absorption band at 632 cm⁻¹ was the Cu-O stretching vibrations of Cu₂O. For the amino-functionalized Cu₂O, it was noted that the two absorption peaks at 2966 cm⁻¹ and 1482 cm⁻¹ were ascribed to stretching and deformation vibration of C-H group, respectively. The characteristic band at 1084 cm⁻¹ could be caused by C-N stretching vibrations, while the peak at 956 cm⁻¹ was from the deformation vibration of N-H. After the amination, the amino groups of the amino-modified Cu₂O octahedrons and Ab₂ can be linked by the crosslinking reaction with the aid of glutaraldehyde, which was clearly stated by UV-vis spectra. In Fig. 1h, as for the absorption spectrum of Ab₂, the peak at about 280 nm is observed, corresponding to the characteristic absorption peak of protein [31], while Cu₂O octahedrons showed no peak in the whole range. As for the spectrum of Cu₂O@Ab₂, the characteristic absorption peak of protein was

detected. Therefore, Ab₂ was successfully modified on Cu₂O octahedrons.

Characterization of Au NBPs

The classical seed-mediated growth strategy was used to prepare Au NBPs with a few alterations [29]. In addition to Au NBPs, the products also contained some gold nanoparticles (Au NSs) (Fig. 2b). It is hard to separate them with simple centrifugation. Hence, as shown in Fig. 2a, in order to obtain pure Au NBPs, the products were purified by the growth of silver shell, distinct depletion interaction between surfactant micelles, and the etching of silver shell. First, the mixture formed a completely distinct morphology with the growth of silver shell including the core-shell rod structure of Au@Ag NRs (Fig. 2c) and spherical structure of Au@Ag NSs. Second, according to various shapes, the Au@Ag NRs were gathered and precipitated at the bottom of the bottle, while the Au@Ag NSs were still suspended in the supernatant; thus, the product was well separated. Finally, in Fig. 2d, the purified Au NBPs with fine monodispersity can be obtained after etching the Ag shell by NH₃·H₂O and H₂O₂.

The purification was further studied by recording the LSPR peak shift in the UV-vis absorption spectrum. In Fig. 2e, the absorption peaks at 684 nm and 525 nm were corresponded to the longitudinal LSPR of Au NBPs and plasmon resonance of Au NSs, respectively. After the growth of silver shell, the product presented two characteristic absorption bands located at 618 nm and 350 nm, which can be due to the longitudinal and transverse SPR of Au@Ag NRs, respectively. Finally, after purification, two new absorption peaks at about 684 nm and 510 nm were the longitudinal and transverse LSPR peaks of Au

Fig. 2 (**a**) Schematic purification of Au NBPs. TEM images of (**b**) Au NPs, (**c**) Au@Ag NRs, and (**d**) Au NBPs. (**e**) UV-vis spectra of as-prepared Au NPs, Au@Ag NRs, and Au NBPs. (**f**) Absorption spectra of Au NBPs after storage for 7, 14, and 21 days
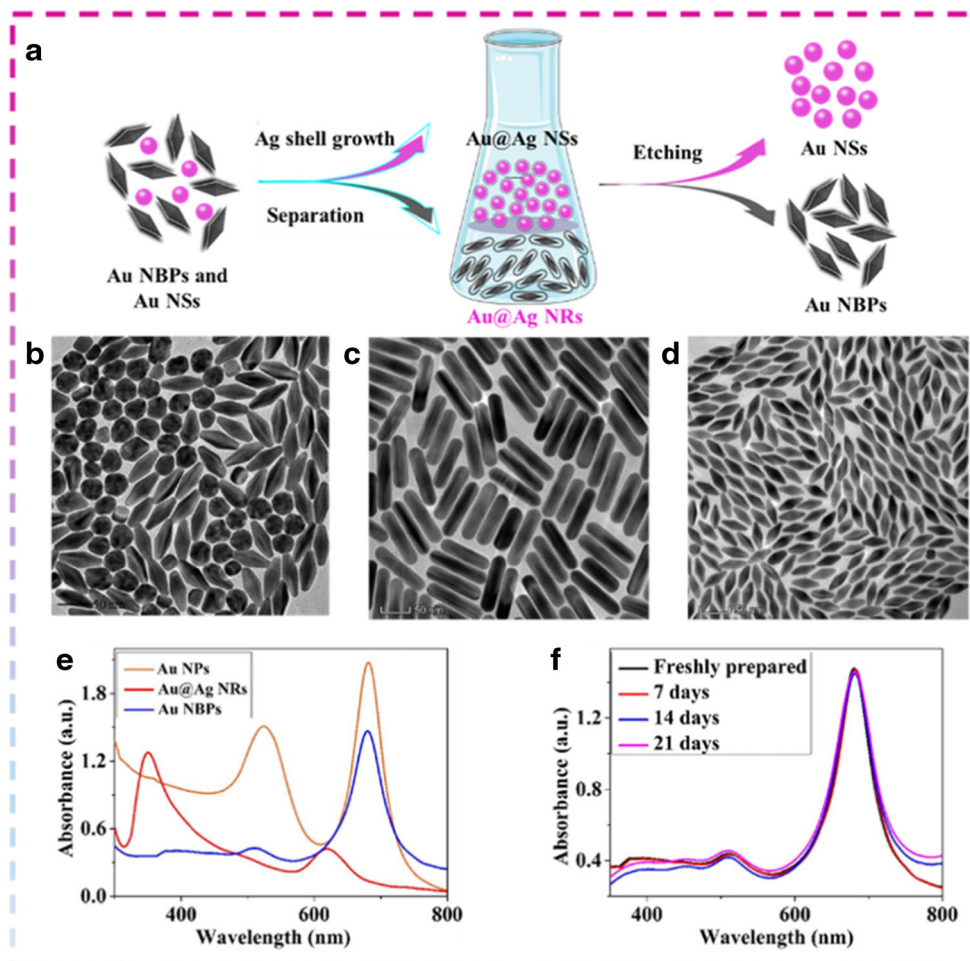
NBPs, respectively. Consequently, the purified Au NBPs had satisfactory monodispersity, desirable size, sharp tips, distinct local field enhancement, and a tunable LSPR band [32]. Furthermore, the wavelength and intensity of plasmon peak exhibited negligible changes within 21-day storage, indicating the long-term stability of the Au NBPs (Fig. 2f).

Principle of the multi-colorimetric immunoassay

Firstly, the mimetic enzymatic reaction of Cu_2O octahedrons was investigated. As in Fig. S2, Cu_2O octahedrons can rapidly catalyze colorless TMB (Fig. S2-a) to blue TMB^+ with the help of H_2O_2-mediated oxidation. The TMB^+ solution had an absorbed peak at 652 nm (Fig. S2-b). After adding HCl to terminate the mimetic enzymatic reaction, the color can instantaneously change from blue TMB^+ to yellow TMB^{2+}, accompanied by an absorption peak at 450 nm (Fig. S2-c).

Additionally, the mechanism of the multi-colorimetric immunoassay was further demonstrated by TEM images and corresponding statistical analysis of Au NBPs after etching with different concentrations of TMB including 0, 0.7, 8,

and 17 mM. In Fig. 3a–d, with the increase in TMB concentration, the shape of Au NBPs changed from bipyramid into almonds-like, walnut-like, and quasi-spherical. The corresponding TEM statistical analysis showed that the length of Au NBPs decreased gradually from 45 to 15 nm, while the inset images further verified the color change of the corresponding solution. Simultaneously, in Fig. S3, the LSPR peaks of Au NBPs blue shifted from 674 to 552 nm when the TMB concentration changed.

Scheme 1 represented the sensing mechanism of the colorimetric method for OTA detection. Specifically, a certain amount of antigen was fixed in 96-well microplate, and then a mixture containing different concentrations of OTA and limited Ab_1 was added; therefore, the immobilized antigen and free OTA can competitively combine with Ab_1. The higher concentration of OTA, the less Ab_1 immobilized. Correspondingly, less Cu_2O-Ab_2 conjugate was fixed to produce less TMB^{2+}. Simultaneously, Au NBPs can be selectively etched to various degrees by different concentrations of TMB^{2+}, causing vivid color changes of the mixture, which can be discriminated by naked eyes at a glance. The rich-colored optical signals were corresponded to different OTA
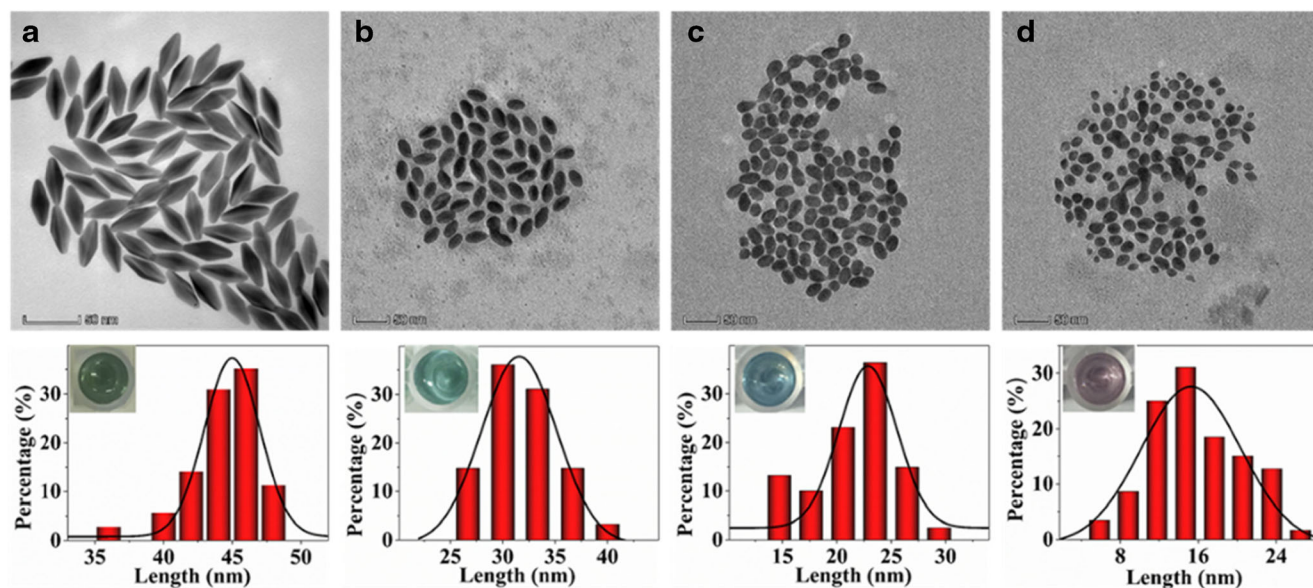
Fig. 3 TEM images and corresponding statistical analysis of Au NBPs after etching in the presence of different TMB concentrations catalyzed by Cu_2O octahedrons. TMB concentrations: (**a**) 0, (**b**) 0.7, (**c**) 8, and (**d**) 17 mM. Insets: the photos of the corresponding solutions

concentrations, accompanied by the notable LSPR peak blue shift of Au NBPs. Thus, a simple and multi-colorimetric immunoassay was fabricated for the detection of OTA.

Optimization of the experimental conditions

According to the mechanism of multi-colorimetric immunosensor, the optimization of experimental conditions was performed by two steps. First, the catalytic activity of Cu_2O octahedrons is important, which can directly determine the yield of TMB^{2+} and the etching performance of Au NBPs. As a consequence, the effect from the conditions such as pH of HAc-NaAc buffer, H_2O_2 concentration, reaction time, and TMB concentration was investigated in detail. The UV-vis absorption intensity at 450 nm was positively correlated with TMB^{2+}

concentration, which was chosen as the indicator of the catalytic activity of Cu_2O. In this study, an interesting observation can be found. As shown in Fig. S4a and S4b, when the solution is in acidic conditions, H_2O_2 can oxidize TMB without mimetic enzyme. Meanwhile, the solution had strong absorption intensity at about 450 nm, accompanied by a visible color variation. When the pH value of the solution was above 6.0, the solution was colorless, and no adsorption peak can be found. Thus, in order to avoid the influence of self-reaction caused by H_2O_2 and TMB in acid condition, the optimization of pH value started from 6.0 (Fig. 4a). The absorption intensity exhibited a maximum at the pH value of around 6.0 and then decreased with the increase in pH value. These results suggested that the catalytic activity of Cu_2O octahedrons reduced in basic solution. Therefore, the appropriate

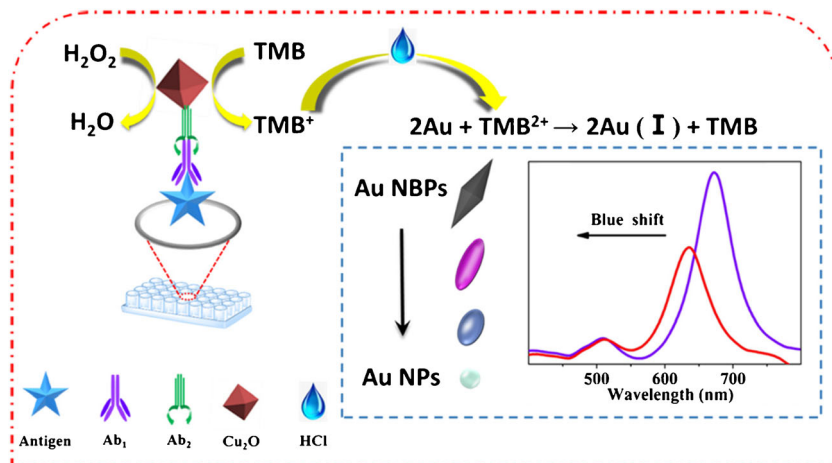**Scheme 1** Schematic diagram of multi-colorimetric immunoassay for OTA detection

Fig. 4 Effect on the catalytic ability of Cu$_2$O octahedrons by (**a**) the pH of HAc-NaAc buffer, (**b**) H$_2$O$_2$ concentration, (**c**) the reaction time, and (**d**) TMB concentration. Effect on the etching for Au NBPs by CTAB concentration (**e**) and etching time (**f**). Error bars represent the standard error derived from three repeated detections
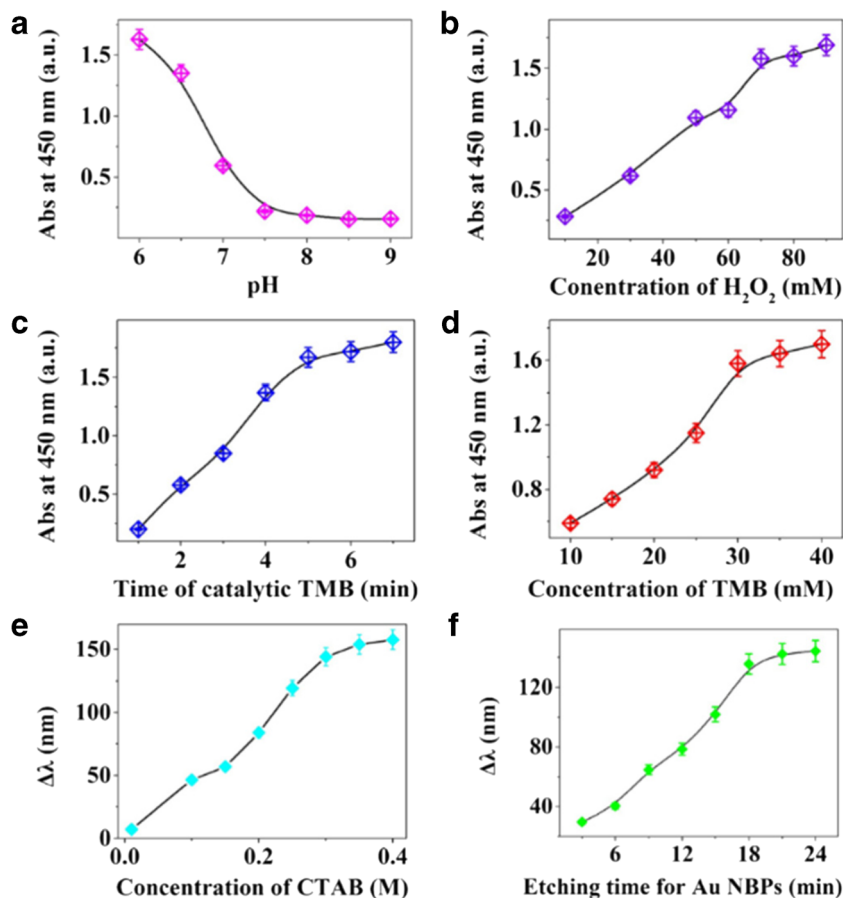
pH value for the catalysis of Cu$_2$O octahedrons was 6.0. Figure 4b showed the effect of H$_2$O$_2$ concentration on the catalytic activity of Cu$_2$O octahedrons. The absorption intensity increased markedly and then reached a bottleneck at 70 mM. So, 70 mM was selected for the subsequent detection. Figure 4c was the influence of reaction time on the catalytic ability of Cu$_2$O octahedrons, showing that the absorption intensity enhanced rapidly and then reached a parallel level at 5 min. Thus, the catalytic time was set at 5 min. In Fig. 4d, the absorption intensity increased rapidly with the increase in the TMB concentration. When it was higher than 30 mM, the absorption intensity increased mildly. In addition, it was obvious that a great sum of flocculent substance formed when the TMB concentration was higher than 30 mM. Therefore, 30 mM was selected as the optimal TMB concentration.

Second, the effect of CTAB concentration and TMB^{2+} etching time were studied in detail. Δλ, the change for the LSPR peak position of Au NBPs, was set as the indicator of the morphological variation of Au NBPs. In Fig. 4e, it can be found that Δλ value increased with the increment of CTAB concentration and reached a parallel level at 0.3 M. Hence, the optimal CTAB concentration was selected as 0.3 M. Figure 4f showed the effect of TMB^{2+} etching time on Δλ, where it

increased gradually and then reached a platform at 18 min. Thus, 18 min of the etching time was selected.

The performance of the multi-colorimetric immunoassay

The concentrations of OTA are related to the blue shift degree of the LSPR peak and the color change. Hence, the performance of the multi-colorimetric immunosensor was implemented by using different concentrations of OTA under the optimum conditions. According to the competitive mode, the free OTA can compete with the fixed antigens on the microplate to combine with the limited amount of antibody. The higher the OTA concentration, the less amount of Cu$_2$O@Ab$_2$ on the microplate; thus, the produced TMB^{2+} decreased gradually. Subsequently, it exhibited a vivid color corresponding with the TMB^{2+} concentration, which can be readily observed by the naked eyes. As in Fig. 5a, the LSPR peak position exhibited blue shift with the decrease of OTA concentration; thus, a series of distinct color transitions can be conveniently and intuitively distinguished by the naked eyes (Fig. 5c). In Fig. 5b, Δλ was demonstrated to be a good linear relationship with the logarithm of OTA concentrations in a range from 5 μg/L to 1 ng/L. The calibration equation was
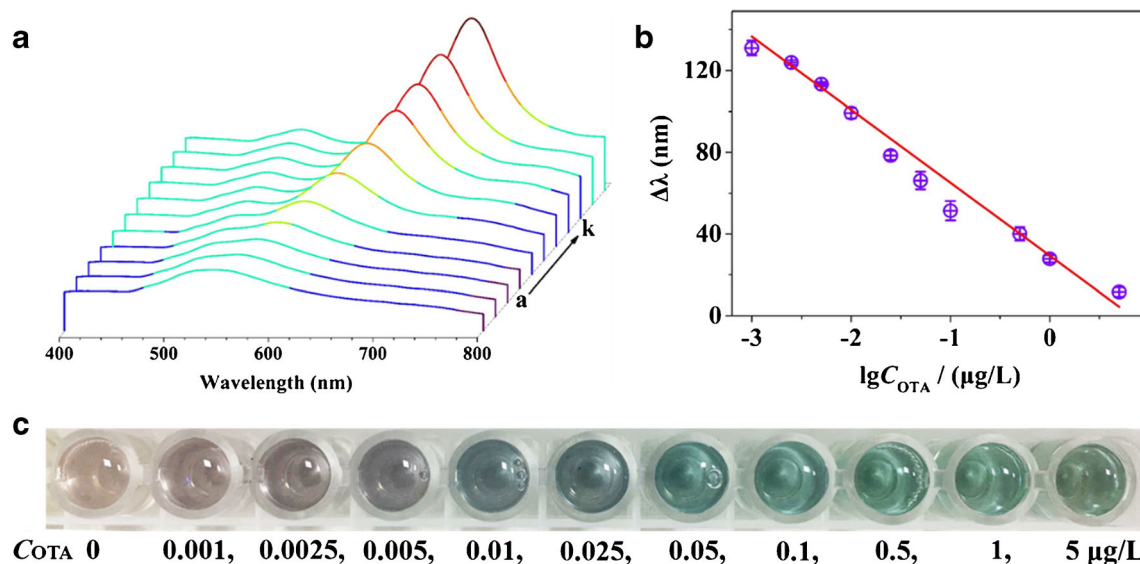
Fig. 5 (a) UV-vis spectra for different concentrations of OTA, (a) 0, (b) 0.001, (c) 0.0025, (d) 0.005, (e) 0.01, (f) 0.025, (g) 0.05, (h) 0.1, (i) 0.5, (j) 1, and (k) 5 μg/L. (b) Calibration curve based on the UV-vis spectra. (c) Photographs of the colorimetric immunoassay at different concentrations of OTA

$\Delta\lambda = 29.37$–$35.74[\log C_{OTA}$ (μg/L)] with an estimated limit of detection at 0.47 ng/L (S/N = 3), and the regression coefficient was 0.988. In addition, compared with other strategies for OTA detection (Table S1), the proposed multi-colorimetric immunoassay possessed a particular impact on the visual semi-qualitative detection of the analyte and exhibited a wide linear range and sensitive analysis.

The selectivity of OTA detection is a key challenge. In Fig. 6a, the selectivity of the multi-colorimetric immunoassay was investigated by calculating the values of $\Delta\lambda$ and the potential interferences including deoxynivalenol (DON), trichothecenes 2 (T-2), aflatoxin B1 (AFB$_1$), zearalenone (ZEN), microcystin-LR (MC-LR), microcystin-YR (MC-YR), microcystin-RR (MC-RR), and nodularin (Nod). After the addition of the interferents, the signals were nearly the same as that of the blank. However, the shift of $\Delta\lambda$ was remarkably decreased only when OTA was added, indicating that these interferences can hardly affect the detection of OTA. The inset of Fig. 6a was the photograph in the presence of different

interferences, proving that the proposed multi-colorimetric immunoassay had highly specific reaction with OTA. The longtime stability of the strategy was further investigated. As shown in Fig. 6b, after 7 days of storage, the performance of proposed immunosensor basically remained the same as the initial response, implying that the developed immunosensor can maintain sufficient stability for OTA detection. Furthermore, the ionic strength was also investigated. As in Fig. S5, the ionic strength had no influence on the stability of the immunosensor.

To further demonstrate the feasibility and practicality of the established strategy in real sample, the millet samples were obtained from local supermarket and tested by high-performance liquid chromatography before use. Afterwards, based on the standard addition method, a series of standard OTA solutions including 0.001, 0.01, 0.1, and 1 μg/L were added and then analyzed. In Fig. 6c, the recoveries of the developed immunoassay were between 98.6 and 111.4%. Meanwhile, it is worth to note that a vivid color can be found,
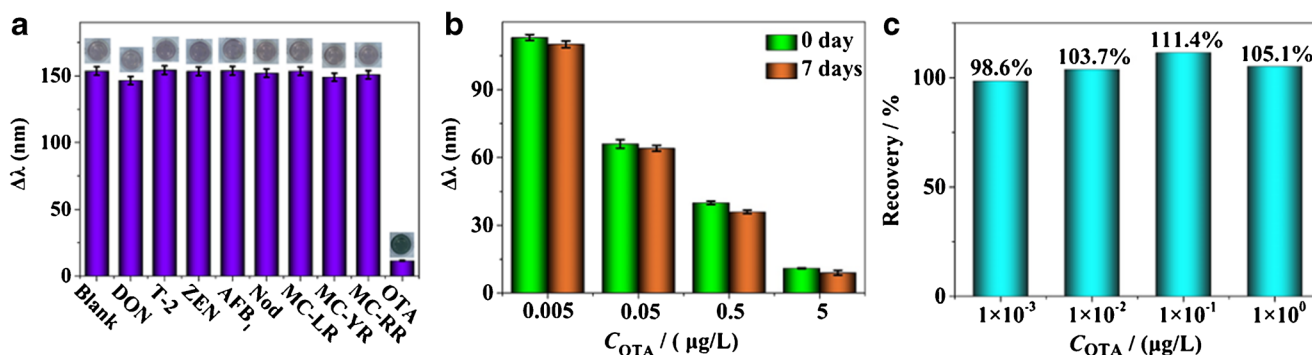

Fig. 6 (a) Selectivity of the multi-colorimetric immunoassay. (b) The longtime stability of the immunoassay. (c) The recoveries of the detection in millet samples

which can not only improve the detection efficiency but also simplify the operation. Hence, the multi-colorimetric immunoassay may have more potential application in the real sample detection.

Conclusion

In summary, a multi-colorimetric immunosensor was established for OTA detection. Peroxidase-like Cu_2O octahedrons were used to label second antibody. Basing on the competitive format, the increase in the OTA concentration can cause a decrease amount of the immobilized $Cu_2O@Ab_2$ and the corresponding decrease in TMB^{2+}, which can affect the etching of Au NBPs and cause blue shift of LSPR peak. Meanwhile, the vivid color changing of the mixture solution can be readily distinguished by the naked eyes. Owing to the high specificity and selectivity, the proposed multi-colorimetric immunoassay was demonstrated to be sensitive in real samples. Furthermore, by replacing different mimic enzymes, this multi-colorimetric strategy could be also extended to detect other biomolecules. However, H_2O_2 in this immunosensor is very vulnerable to environment change and may also cause some damage to biomolecules, which may impede their real analytical application. It will be a new direction to develop efficient oxide mimetic nanozymes.

Compliance with ethical standards

Conflict of interest The author(s) declare that they have no competing interest.

References

1. Fan SS, Zhao MG, Ding LJ, Li H, Chen SG (2017) Preparation of Co_3O_4/crumpled graphene microsphere as peroxidase mimetic for colorimetric assay of ascorbic acid. Biosens Bioelectron 89:846–852

2. Liu YS, Wang J, Zhao C, Guo XX, Song XL, Zhao W, Liu SJ, Xu K, Li J (2019) A multicolorimetric assay for rapid detection of Listeria monocytogenes based on the etching of gold nanorods. Anal Chim Acta 1048:154–160

3. Ma XM, Lin Y, Guo LH, Qiu B, Chen GN, Yang HH, Lin ZY (2017) A universal multicolor immunosensor for semiquantitative visual detection of biomarkers with the naked eyes. Biosens Bioelectron 87:122–128

4. Chen ZH, Chen CQ, Huang HW, Luo F, Guo LH, Zhang L, Lin ZY, Chen GN (2018) Target-induced horseradish peroxidase deactivation for multicolor colorimetric assay of hydrogen sulfide in rat brain microdialysis. Anal Chem 90:6222–6228

5. Liu WP, Gan CF, Chang WD, Qileng A, Lei HT, Liu YJ (2019) Double-integrated mimic enzymes for the visual screening of microcystin-LR: copper hydroxide nanozyme and G-quadruplex/hemin DNAzyme. Anal Chim Acta 1054:128–136

6. Ma XM, Chen ZT, Kannan P, Lin ZY, Qiu B, Guo LH (2016) Gold nanorods as colorful chromogenic substrates for semiquantitative detection of nucleic acids, proteins, and small molecules with the naked eye. Anal Chem 88:3227–3234

7. Li MJ, Huang XX, Yu HL (2019) A colorimetric assay for ultrasensitive detection of copper (II) ions based on pH-dependent formation of heavily doped molybdenum oxide nanosheets. Mater Sci Eng C 101:614–618

8. Meinzer N, Barnes WL, Hooper IR (2014) Plasmonic meta-atoms and metasurfaces. Nat Photonics 8:889–898

9. Guo LH, Jackman JA, Yang HH, Chen P, Cho NJ, Kim DH (2015) Strategies for enhancing the sensitivity of plasmonic nanosensors. Nano Today 10:213–239

10. Zhou W, Gao X, Liu DB, Chen XY (2015) Gold nanoparticles for in vitro diagnostics. Chem Rev 115:10575–10636

11. Lin Y, Zhao MM, Guo YJ, Ma XM, Luo F, Guo LH, Qiu B, Chen GN, Lin ZY (2016) Multicolor colormetric biosensor for the determination of glucose based on the etching of gold nanorods. Sci Rep 6:37879

12. Saa L, Coronado-Puchau M, Pavlov V, Liz-Marzan LM (2014) Enzymatic etching of gold nanorods by horseradish peroxidase and application to blood glucose detection. Nanoscale 6:7405–7409

13. Ye XC, Jin LH, Caglayan HR, Chen J, Xing GZ, Zheng C, Doan-Nguyen V, Kang YJ, Engheta N, Kagan CR, Murray CB (2012) Improved size-tunable synthesis of monodisperse gold nanorods through the use of aromatic additives. ACS Nano 6(3):2804–2817

14. Vigderman L, Khanal BP, Zubarev ER (2012) Functional gold nanorods: synthesis, self-assembly, and sensing applications. Adv Mater 24:4811–4841

15. Xu SH, Ouyang WJ, Xie PS, Lin Y, Qiu B, Lin ZY, Chen GN, Guo LH (2017) Highly uniform gold nanobipyramids for ultrasensitive colorimetric detection of influenza virus. Anal Chem 89:1617–1623

16. Xu SH, Jiang LP, Nie YY, Wang J, Li HM, Liu YY, Wang W, Xu GY, Luo XL (2018) Gold nanobipyramids as dual-functional substrates for in situ "turn on" analyzing intracellular telomerase activity based on target-triggered plasmon enhanced fluorescence. ACS Appl Mater Interfaces 10:26851–26858

17. Bulbul G, Hayat A, Andreescu S (2015) A generic amplification strategy for electrochemical aptasensors using a non-enzymatic nanoceria tag. Nanoscale 7:13230–13238

18. Wang Y, Liu F, Wang LQ, Wang Q, Selvaraj JN, Zhao YJ, Wang Y, Xing FG, Liu Y (2018) The pH signaling transcription factor aopacC regulates ochratoxin A biosynthesis in *aspergillus ochraceus*. J Agric Food Chem 66:4394–4401

19. Fu GL, Sanjay ST, Zhou W, Brekken RA, Kirken RA, Li XJ (2018) Exploration of nanoparticle-mediated photothermal effect of TMB-HO colorimetric system and its application in a visual quantitative photothermal immunoassay. Anal Chem 90:5930–5937

20. Zhan YJ, Zeng YB, Li L, Guo LH, Luo F, Qiu B, Huang YJ, Lin ZY (2020) Cu^{2+}-modified boron nitride nanosheets-supported subnanometer gold nanoparticles: an oxidase-mimicking nanoenzyme with unexpected oxidation properties. Anal Chem 92:1236–1244

21. Tao YF, Xie SY, Xu FF, Liu AM, Wang YX, Chen DM, Pan YH, Huang LL, Peng DP, Wang X, Yuan ZH (2018) Ochratoxin A: toxicity, oxidative stress and metabolism. Food Chem Toxicol 112:320–331

22. Karczmarczyk A, Reiner-Rozman C, Hageneder S, Dubiak-Szepietowska M, Dostalek J, Feller KH (2016) Fast and sensitive detection of ochratoxin A in red wine by nanoparticle-enhanced SPR. Anal Chim Acta 937:143–150

23. Intertional Agency for Research on Cancer (IARC) (1993) Some naturally occurring substances: food items and constituents, heterocyclic aromatic amines and mycotoxins. IARC Monogr Eval Carcinog Risks Hum 56:245–395

24. Irakli MN, Skendi A, Papageorgiou MD (2017) HPLC-DAD-FLD method for simultaneous determination of mycotoxins in wheat bran. J Chromatogr Sci 55(7):690–696

25. Zhang RS, Xu H, Wang WL, Zhan RT, Chen WW (2014) Simultaneous determination of aflatoxin B1, B2, G1, G2, ochratoxin A, and sterigmatocystin in traditional Chinese medicines by LC-MS-MS. Anal Bioanal Chem 406:3031–3039

26. Pittet A, Royer D (2002) Rapid, low cost thin-layer chromatographic screening method for the detection of ochratoxin A in green coffee at a control level of 10 μg/kg. J Agric Food Chem 50:243–247

27. Amelin VG, Karaseva NM, Tretyakov AV (2013) Simultaneous determination of trichothecene mycotoxins, ochratoxin A, and zearalenone in grain and products of its processing, feed premixes, and meat by gas chromatography. J Anal Chem 68(1):61–67

28. Shaik TA, Alfonso-Garcia A, Zhou XN, Arnold KM, Haudenschild AK, Krafft C, Griffiths LG, Popp J, Marcu L (2020) FLIm-guided Raman imaging to study cross-linking and calcification of bovine pericardium. Anal Chem 92:10659–10667

29. Wei J, Chen HM, Chen HH, Cui YY, Qileng A, Qin WW, Liu WP, Liu YJ (2019) Multifunctional peroxidase-encapsulated nanoliposomes: bioetching-induced photoelectrometric and colorimetric immunoassay for broad-spectrum detection of ochratoxins. ACS Appl Mater Interfaces 11:23832–23839

30. Zhang DF, Zhang H, Guo L, Zheng K, Han XD, Zhang Z (2009) Delicate control of crystallographic facet-oriented Cu_2O nanocrystals and the correlated adsorption ability. J Mater Chem 19:5220–5225

31. Larson NR, Wei YJ, Middaugh CR (2018) Label-free, direct measurement of protein concentrations in turbid solutions with an UV-visible integrating cavity absorbance spectrometer. Anal Chem 90: 4982–4986

32. Chang J, Zhang AM, Huang ZC, Chen YS, Zhang Q, Cui DX (2019) Monodisperse Au@Ag core-shell nanoprobes with ultrasensitive SERS activity for rapid identification and Raman imaging of living cancer cells. Talanta 198:45–54